Journal of Advanced Research xxx (xxxx) xxx

Contents lists available at ScienceDirect

Journal of Advanced Research

journal homepage: www.elsevier.com/locate/jare

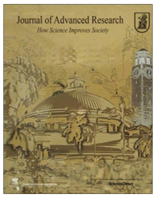

Original Manuscript

Design of a sustained-release nanosystem for ultra-efficient absorption of anthocyanins and regulating lung damage through the “lung-gut” axis

Jin-Long Tian [a], Nuo Wang [a], Qin-Fu Zhao [b], Zhi-Huan Zang [a], Zhi-Ying Li [a], Zhen-Yu Wang [e], Ying Zhou [c], Bao-Ru Yang [c], Sergey S. Makarov [d], Anton I. Chudetsky [d], Liang Wang [f], Ying He [f], Bin Li [a,*]

[a] *College of Food Science, Shenyang Agricultural University, National R&D Professional Center for Berry Processing, National Engineering and Technology of Research Center for Small Berries, Key Laboratory of Healthy Food Nutrition and Innovative Manufacturing, Shenyang, Liaoning Province 110866, China*
[b] *Department of Pharmaceutics, School of Pharmacy, Shenyang Pharmaceutical University, 103 Wenhua Road, Shenyang, Liaoning Province 110016, China*
[c] *Food Sciences, Department of Life Technologies, University of Turku, Turku, Finland*
[d] *Moscow Timiryazev Agricultural Academy, Russian State Agrarian University, Moscow 127550, Russia*
[e] *School of Chemistry and Chemical Engineering, Harbin Institute of Technology, Harbin, China*
[f] *Zhejiang Lanmei Technology Co., Ltd., Zhuji, Zhejiang 311800, China*

HIGHLIGHTS

- The anthocyanin nanodelivery system CLS with “molecular cap” protection was constructed.
- The design and absorption behavior of CLS are guided by computational chemistry.
- CLS increased anthocyanin absorption into blood >13 times and lung enrichment >25 times.
- CLS exhibits significant oral lung targeting and intestinal sustained-release effects.

GRAPHICAL ABSTRACT

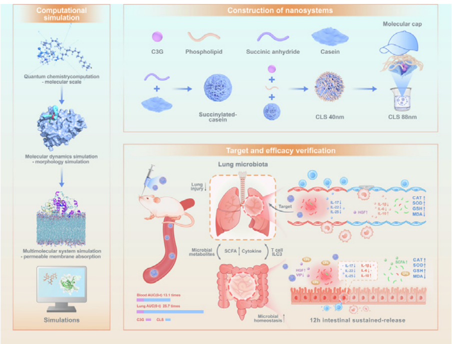

ARTICLE INFO

Article history:
Received 3 February 2025
Revised 15 May 2025
Accepted 29 May 2025
Available online xxxx

Keywords:
Anthocyanins
Nanodelivery
Bioavailability
Lung enrichment
Pharmacokinetics

ABSTRACT

Introduction: Anthocyanins have various health benefits but are limited by fast elimination and low bioavailability. Many studies have shown that nano delivery systems are effective in improving the intestinal absorption and bioavailability of anthocyanins. However, in the process of selecting anthocyanin nanomaterials, a dilemma is faced: numerous functional nanomaterials lack edible properties, it is difficult to meet the edible and functional requirements of nanomaterials simultaneously. Therefore, it is necessary and inevitable to select nano-anthocyanin carriers that are edible and have certain functional and morphological characteristics.

Objectives: The study aim to provide an efficient, sustained-release and easy to industrialize nanosystem method to solve the problem of low bioavailability of anthocyanins.

Methods: A succinylated casein-phospholipid-anthocyanin nanosystem (CLS) was designed via computational chemistry-guided one-step self-assembly. Morphological, *in vitro/in vivo* digestion, pharmacokinetic were conducted. Furthermore, the effects of CLS on intestinal microecology were verified by using enteritis model animals, and the lung-targeting effect of CLS on lung health was verified by using lung injury model animals.

---

* Corresponding author.

E-mail addresses: 2017500015@syau.edu.cn (J.-L. Tian), 2023240298@stu.syau.edu.cn (N. Wang), qinfuzhao@syphu.edu.cn (Q.-F. Zhao), zzh22h@163.com (Z.-H. Zang), 2020200015@stu.syau.edu.cn (Z.-Y. Li), yizhou@utu.fi (Y. Zhou), baoru.yang@utu.fi (B.-R. Yang), s.makarov@rgau-msha.ru (S.S. Makarov), chudetski@rgau-msha.ru (A.I. Chudetsky), wangl@medelley.com (L. Wang), hey@medelley.com (Y. He), libinsyau@163.com (B. Li).

https://doi.org/10.1016/j.jare.2025.05.059

Please cite this article as: J.-L. Tian, N. Wang, Q.-F. Zhao et al., Design of a sustained-release nanosystem for ultra-efficient absorption of anthocyanins and regulating lung damage through the “lung-gut” axis, Journal of Advanced Research, https://doi.org/10.1016/j.jare.2025.05.059

Results: CLS exhibited 24-hour intestinal sustained release and lung-targeted enrichment. Pharmacokinetic studies showed 25.7-fold higher lung $AUC_{(0\text{-}t)}$ and 13.1-fold higher blood $AUC_{(0\text{-}t)}$ compared to free anthocyanins. CLS significantly alleviated lung injury and colitis in model rats via the gut-lung axis.

Conclusion: This study significantly improved the bioavailability of anthocyanins and demonstrated the oral lung-targeting function of anthocyanins for the first time, paving the way for utilizing anthocyanins as dietary supplements and precision nutrition.

Introduction

Anthocyanins are important water-soluble pigments in plants and are commonly found in flowers, leaves, stems and pericarp [1]. These compounds are secondary metabolites involved in plant stress resistance [2]. Anthocyanins are generally synthesized in the cytoplasm and endoplasmic reticulum of cells and are subsequently transported to vacuoles, where they are stained red, blue, purplish red or purplish black [3]. In addition, anthocyanins impart colorful colors to plant organs and can attract insects to spread pollen, which is conducive to seed formation and propagation and to offspring breeding [4]. With the dietary intake of plant-derived foods rich in anthocyanins, it was further found that anthocyanins have a variety of physiological health care functions, such as scavenging free radicals in the body [5], exerting antitumor effects [6], protecting the liver [7] and lungs [8], preventing diabetes [9], protecting eyesight [10] and improving Alzheimer's disease [11]. Therefore, an increasing number of people are paying attention to the anthocyanin diet. From the perspective of resident diet and recommended intake, the intake of anthocyanins in the diet of American residents is approximately 12.5–42.8 mg/d, the intake of European Union residents is approximately 18.7–64.9 mg/d, and the intake of Chinese residents is approximately 9.6–43.1 mg/d, all of which demonstrate the importance of anthocyanins for nutritional health [12,13]. However, the bioavailability of anthocyanins *in vivo* is extremely low [14]. Studies have shown that the biological concentration of anthocyanins in plasma is generally approximately 1 % of the total consumption, the blood absorption $t_{1/2}$ is only approximately 0.5 h, and almost all of these compounds are eliminated in 2 h [15]. The low absorption rate of anthocyanins leads to ineffective use of their functions, which seriously restricts the nutritional value of anthocyanin-rich foods [16]. Therefore, conducting research on the biological absorption of anthocyanins and finding effective methods to improve their bioavailability are the keys to realizing the nutritional value of foods rich in anthocyanins, and this topic is currently popular and difficult.

In recent years, many studies have shown that nanodelivery systems are effective at improving the intestinal absorption and bioavailability of anthocyanins [17]. Nanodelivery carriers are widely used in food, medicine and chemistry due to their high bioavailability and ability to enhance the sustained release, targeting and controllability of loaded active molecules [18,19]. In the process of selecting anthocyanin nanomaterials, we are faced with a dilemma: (I) To pursue the targeting and functionality of nanosystems, use inedible materials for loading and modification; (II) To meet the requirements of edibility, food materials were selected as carriers, but they failed to achieve good morphological characteristics (particle size, PDI, etc.), functional characteristics and targeting characteristics. Therefore, choosing a carrier for anthocyanin nanosystems, which are both edible and have certain functional and morphological characteristics, is necessary and is an inevitable development trend.

The fundamental reason for the low bioavailability of anthocyanins is the presence of 2-phenyl benzopyrilium (flavylium) salts on the C-ring of their molecular structure [26]. This results in anthocyanins exhibiting strong hydrophilicity (logP < 1) and poor cell penetration ability (tPSA > 120), making it difficult for anthocyanins to penetrate the absorption barrier (mucus layer and phospholipid bilayer) into the bloodstream [1]. Therefore, the design and development of anthocyanin absorption and delivery systems are vastly different from those of other liposolubilizing natural active molecules, such as curcumin [27], astaxanthin [19], and resveratrol [28]. Improving the solubility of anthocyanins should be the first problem to be considered, followed by the difficulty of accessing the positive charge of the anthocyanin structure through the electronegative small intestinal mucus layer and the electronegativity of nanocarriers[25]. To increase the application value of the anthocyanin nanodelivery system, the simplicity of the process should also be considered.

Herein, this study selected amphiphilic phospholipids as the material for improving lipid solubility. In our previous study, casein was found to be an ideal skeleton material for anthocyanin delivery [26]. To make the system ultimately negatively charged, casein was acylated and modified. The succinylated casein-phospholipid-anthocyanin nanosystem (CLS) was designed and constructed by a one-step self-assembly method with the help of computational chemistry simulation. Moreover, morphological characterization, nanosystem force analysis, *in vitro* simulated digestion and absorption, and *in vivo* and *in vitro* absorption and uptake experiments of CLS were carried out, focusing on the intestinal absorption of CLS and its influence on the gut microbiota, and the targeted enrichment of CLS was analyzed by fluorescence imaging and pharmacokinetics. Furthermore, the effects of CLS on intestinal microecology were verified by using enteritis model animals, and the lung-targeting effect of CLS on lung health was verified by using lung injury model animals. This study provides an efficient, sustained-release and easy to industrialize nanosystem method to solve the problem of low bioavailability of anthocyanins (Scheme 1).

Materials and methods

Chemicals

Casein (CAS 9000-71-9), succinic acid (CAS 110-15-6), lecithin (CAS 8002-43-5), fluorescein isothiocyanate (FITC, CAS 27072-45-3), trypsin (CAS 9002-07-7), pepsin (CAS 9001-75-6), 4′,6-diamidino-2-phenylindole (DAPI, CAS 28718-91), thiazole blue (MTT, CAS 298-93-1), and sodium hydroxide (NaOH, CAS 1310-73-2) were purchased from Shanghai Aladdin Biochemical Technology Co., Ltd. Cyanidin-3-glucoside (C3G) was prepared in our laboratory (purity ≥ 95 %) from 'Lanmei 1′ blueberry anthocyanins extract (Zhejiang Lanmei Technology Co., Ltd, Zhuji, China). A DMSO-d_6 (CAS 2206–27-1) solution was obtained from Sigma-Aldrich (USA).

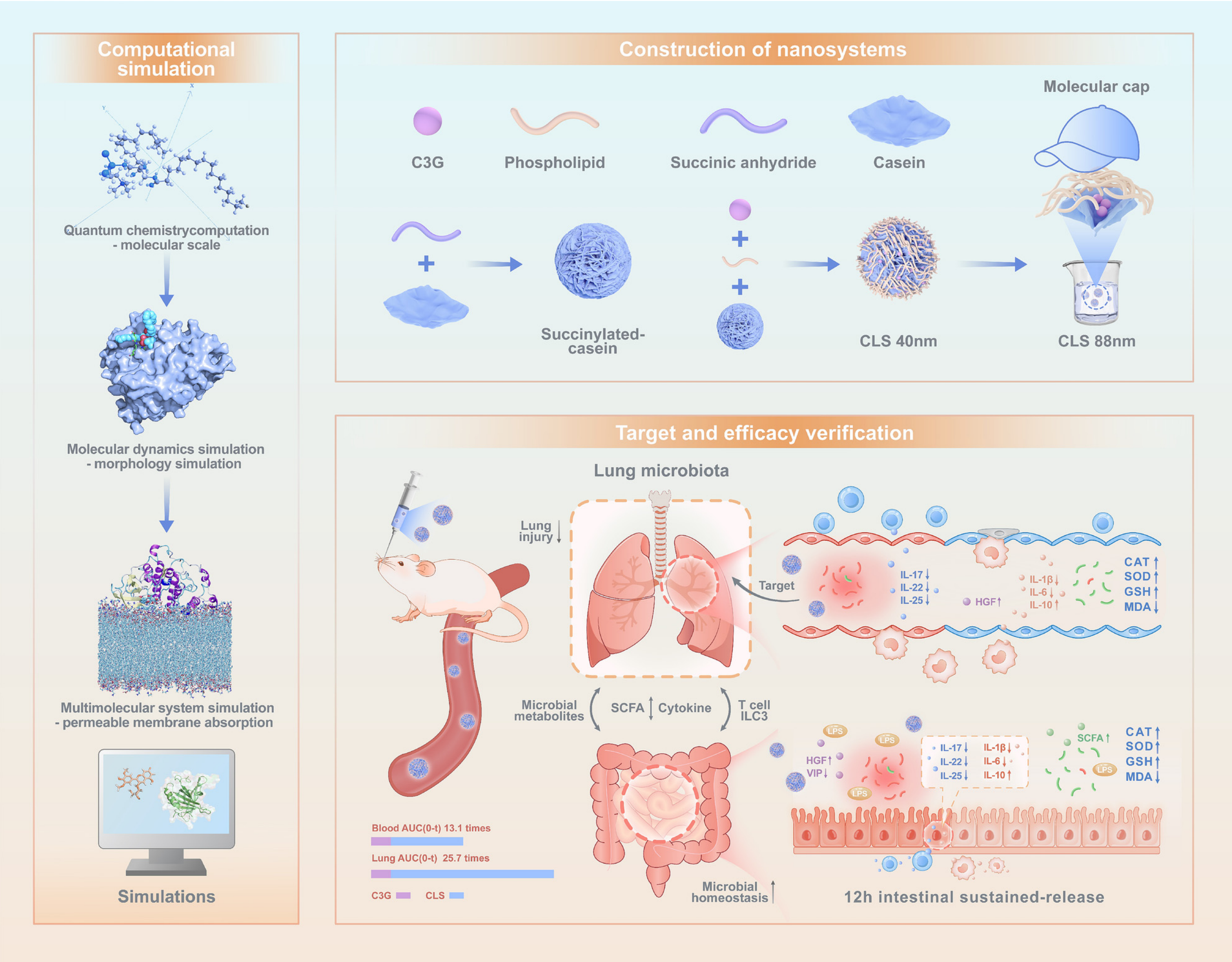

Scheme 1. Under the guidance of computational simulation, the oral anthocyanin nanosystem with lung targeting and intestinal sustained-release functions was constructed and its efficacy was verified.

Screening of carrier materials based on computational chemistry assistance

The protein selection materials included common food grade proteins such as casein, soy protein, bovine serum protein, peanut protein, albumin, gluten, whey protein, collagen, egg white protein, soy protein, lactoferrin, phycocyanin, silkworm pupa protein, rice protein, and lactoglobulin. The lipid classification system proposed by the "Lipid Metabolism Pathway Research Program" funded by the National Institutes of Health (NIH) [29] in 2003 divides lipids into eight major categories: fatty acids, glycerolipids, glycerophospholipids, sphingolipids, sterol lipids, preenol lipids, saccharolipids and polyketides. Then, molecular simulation studies were conducted on the selected proteins and lipids with C3G, as detailed in the Supporting Information.

Preparation of succinylated casein (SCN)

Casein (0.5 g) was dispersed in 40 mL of NaOH (0.04 mol/L), and 80 mL of pH 7.4 PBS was subsequently added and stirred at 65 °C for 2 h. Succinic anhydride (375 mg, dissolved in 10 mL of pH 7.4 PBS) was slowly added dropwise while stirring. After 1 h, 2 M NaOH was added, and the pH was adjusted to 8.5. After stirring for 30 min, the reaction ended. The reaction mixture was dialyzed at 4 °C for 24 h, during which the water was changed 3 times, and after freeze-drying, the mixture was stored at 4 °C for later use.

Characterization of casein and SCN

Casein and SCN were dissolved in buffer solutions with different pH values (pH 3–8), and the changes in zeta potential were subsequently measured via a nanoparticle size potentiometer (Nano-ZS90, Malvern, UK). Casein (10 mg) and SCN (10 mg) were dissolved in DMSO-d_6 solution and transferred to NMR tubes. Bruker ARX-300 spectrometers (Zürich, Switzerland) were used to acquire ^{1}H NMR spectra with tetramethylsilane (TMS) serving as an internal standard.

One-step self-assembly of anthocyanin nanoparticles

For preparation of the phospholipid solution, 200 mg of phospholipids was weighed, 20 mL of ethanol was added, and the mixture was ultrasonicated for 5 min. Prepare SCN solution: weigh 15 mg SCN, add 7.5 mL ultrapure water, and ultrasonic for 5 min. C3G-phospholipid (CL) complex preparation steps: 5 mg of anthocyanins were weighed in a vial and dissolved in 1 mL of pH 1.2 HCl. 1 mL of the 10 mg/mL phospholipid solution was added to the vial, which was then incubated in a water bath for 2 h to mix the two thoroughly. C3G-phospholipid with SCN-modified (CLS) complex preparation steps: 5 mg of anthocyanins were weighed in a vial and dissolved in 1 mL of pH 1.2 HCl. 1 mL of the 10 mg/mL phospholipid solution was added to the vial. After the solution was stirred in a water bath at 40 °C for 15 min, 2.5 mL of an ultrapure water (SCN) solution was added, and the mixture was then incubated in a water bath for 2 h to mix the two thoroughly.

Characterizations of the CL and CLS nanocomposites

Transmission electron microscopy (TEM)

The prepared CL and CLS were ultrasonically dispersed to prepare a dispersion with a concentration of approximately 200 μg/mL, after which the sample was dropped onto a copper mesh and dried for TEM characterization.

Atomic force microscopy (AFM)

CL and CLS were dispersed in ultrapure water to prepare a test solution with a concentration of approximately 100 μg/mL, after which the test solution was dispersed onto a mica sheet and allowed to dry naturally, after which the surface morphology of CL and CLS was observed via AFM.

Dynamic light scattering (DLS)

The test sample was dispersed in ultrapure water to prepare a sample solution with a concentration of approximately 100 μg/mL, 1 mL of sample was added to the particle size cup, and the particle size distribution, polydispersity coefficient (PDI) and ζ-potential of the nanoparticles were measured with a Malvern Zetasizer Nano-ZS (Malvern Inst. Ltd., UK).

Circular dichroism (CD) spectroscopy

The SCN, CLS and CL sample solutions were used at a concentration of approximately 200 μg/mL, and the samples were scanned with circular dichroism at 190–300 nm.

Fluorescence spectroscopy

SCN, C3G, CLS and CL solutions with a concentration of 200 μg/mL were used for fluorescence spectroscopy analysis. The excitation wavelength was 280 nm, the emission wavelength was 300–400 nm, and the fluorescence spectrum of the sample was measured at 1 nm/min.

Infrared spectroscopy

The sample and KBr were mixed and pressed in a dry environment, and FT-IR measurements were conducted in the range of 400 cm^{-1}-4000 cm^{-1} with a resolution of 1 cm^{-1}.

UV–Vis spectroscopy

C3G, SCN, CL, and CLS were dissolved in a phosphate buffer solution to prepare a sample solution with a concentration of 100 μg/mL. The sample was subsequently added to a quartz cuvette, after which full-wavelength UV scanning was performed.

Oil-water partition coefficient

10 mL of *n*-octanol solution was added to an equal volume of 10 mL of water. After sealing, the mixture was placed on a magnetic stirrer and stirred at 37 °C for 24 h. Then, the mixture was placed in a separatory funnel and left to stand for several hours, after which the upper layer of water-saturated *n*-octanol and the lower layer of saturated aqueous *n*-octanol were removed for use. C3G, CL and CLS were added to a two-phase solution of 1 mL of water and 1 mL of *n*-octanol (the *n*-octanol phase needs to be saturated with the solution for more than 24 h before the experiment), after which the mixture was shaken well. After reaching distribution equilibrium, the concentrations in the organic phase C_0 and the water phase C_w were measured.

Loading efficiency (LE) and encapsulation efficiency (EE)

10 mL of nanosystem solution was centrifuged at 5000 rpm for 30 min, the filtrate was collected. Then the absorbance was measured using a UV spectrophotometer at a wavelength of 520 nm, and the encapsulation efficiency (EE) was calculated.

15 mg of the nanosystem was weighed and placed in a 100 mL volumetric flask. The solution was diluted to volume with a pH 1.2 hydrochloric acid solution, sonicated for 4 h, and transferred to an ultrafiltration centrifuge tube. The mixture was centrifuged at 5000 rpm for 30 min. The initial filtrate was discarded, and the absorbance was measured using a UV spectrophotometer at a wavelength of 520 nm to calculate the drug loading efficiency (LE).

Oil-water partition coefficient

C3G, CL and CLS were added to a two-phase solution of 1 mL of water and 1 mL of *n*-octanol (the *n*-octanol phase needs to be saturated with the solution for more than 24 h before the experiment). After fully shaking to reach distribution equilibrium, the C3G concentrations in the organic-phase C_0 and the aqueous-phase C_W were measured.

Determination of the saturated solubility of C3G, CL and CLS in n-octanol

Excess C3G, CL and CLS were added to 1 ml of *n*-octanol solution and incubated at 37 °C for 48 h on a shaking table. The supernatant was diluted with *n*-octanol to an appropriate concentration. The blank *n*-octanol was used to measure the absorbance of the supernatant with a spectrophotometer at 536 nm, after which the saturated solubility was calculated.

Nanoparticle element analysis

X-ray photoelectron spectroscopy (XPS) was used to analyze the elemental composition of the nanosystem. A KRATOS Axis Supra photoelectron spectrometer was used, and the excitation light source was Al Kα X-rays (energy 1486.6 eV), power 400 W, and basic vacuum 6×10^{-9} Torr. The C1s spectral line of the externally contaminated carbon was corrected for sample charging effects at 285.0 eV. EScape software was used for data processing.

Verification of the SCN buffer capacity

The SCN was dissolved in ultrapure water, the pH was adjusted to 4 with hydrochloric acid (pH 1.2), different amounts of 0.1 M NaOH solution were added to different solutions, and the pH of the solution was measured with a pH meter.

Nano system buffer capacity test

C3G, CL, and CLS were dispersed in a hydrochloric acid solution (100 μg/mL) at pH 4.0, and different amounts of 0.1 M NaOH solution were added to the solution until the pH was approximately 4–9. The solution was subsequently photographed and observed. The films were tested by using a scanner (n = 9), and the R, G, and B values of the indicated films were obtained. The response sensitivity (S_{RGB}) of sodium hydroxide to the chromaticity of the nanosystem was calculated according to the following equation:

$$\mathbf{S}_{RGB} = \frac{\Delta R + \Delta G + \Delta B}{R + G + B} \times 100\%$$

where R, G, and B are the initial values of red, green and blue, respectively, in C3G and ΔR, ΔG, and ΔB are the differences between CL/CLS and C3G.

Molecular size simulation

C3G, phosphatidylcholine (the main component of phospholipids), and modeled casein were used to calculate the particle size of the nanocomposites. The molecular structures of the small molecules C3G and phosphatidylcholine were optimized by a ChemBiodraw 3D (version 2014) MM^{2+} force field, and simple charge optimization of macromolecular casein was carried out in

Python Molecular Viewer (PyMOL, version 1.8.2). The optimized molecules were simulated and measured by Spartan'24, and the three-dimensional X/Y/Z spatial particle size was obtained.

Molecular dynamics analysis of self-assembled nanosystems

The wild-type target protein was manually mutated using MEGA12.9 to replace Lys, Arg, and Gln residues on the protein surface with amino acids that can react with succinic acid. C3G and PC small molecules were prepared with the ligprep module and flexibly docked using induced fit docking. Mutant proteins were optimized using the Protein Preparation Wizard in Schrödinger, and a grid file defining the docking pocket was generated using the Receptor Grid Generation module in Maestro. The ATP pocket was used as the center of the active pocket, and molecular docking was performed with the Glide docking module using SP precision. Based on the C3G-PC complexes obtained by the above operations, kinetic simulation studies were conducted on C3G-SCN complexes and C3G-PC-SCN complexes using Desmond software. The complexes were dissolved in an SPC solvent box with a periodic boundary size of 10*10*10 Å, and NA+ neutralization system was added. 1000 frames of conformation were simulated and outputted for subsequent analysis.

Simulated digestion and release

C3G release in simulated gastric fluids

50 mg of C3G, CL and CLS were weighed, dispersed in 5 ml of simulated gastric juice (37 °C), and rotated at 125 rpm. After 0.25 h, 0.5 h, 1 h, 2 h, 3 h, 4 h, and 6 h, all the release media were removed, and an equal volume of release media was added at 37 °C. UV absorption was measured at a wavelength of 536 nm.

Release of C3G in simulated intestinal fluids

50 mg of C3G, CL and CLS were weighed and dispersed in 5 mL of simulated intestinal fluid (37 °C) at a speed of 125 rpm. After 0.25 h, 0.5 h, 1 h, 2 h, 4 h, 6 h, 9 h, 12 h, and 24 h, the release medium was removed, and an equal volume of 37 °C simulated intestinal juice release medium was added at the same time. The pH of the removed liquid was adjusted to 1.2 by adding hydrochloric acid, and the UV absorption was measured at a wavelength of 536 nm.

Release of C3G in simulated gastrointestinal fluids

First, 50 mg of CL and CLS samples was weighed and dispersed in 5 mL of simulated gastric juice (37 °C) at a rotation speed of 125 rpm. After 0.25 h, 0.5 h, 1 h, and 2 h, all the release media were removed, and an equal volume of release media was added at 37 °C. UV absorption was measured at a wavelength of 536 nm. After 2 h, an equal volume of 37 °C simulated intestinal fluid release medium was added for the release experiment. The cutoff time was 24 h, and the method was the same as that described above.

Preparation of FITC-labeled CLS samples

The prepared CLS sample was dispersed in PBS buffer and FITC fluorescent dye was added at a mass ratio of 25:1. After reacting for 12 h in the dark, the sample was collected by centrifugation and dialyzed to remove unattached free FITC dye. Caco-2/HepG2 cells were seeded in a 24-well plate and incubated for 24 h. FITC-labeled CLS was added at a concentration of 25 μg/mL in serum-free medium and incubated for different durations. The cells were then washed with PBS, fixed with formaldehyde, stained with DAPI, and observed under a CLSM.

Molecular dynamics calculations of the uptake capacity of CLS and C3G

MD was used to study CLS and C3G penetration of cell membranes. CHARMM 36 force field was used for lipid bilayer simulation. System was equilibrated for 20 ns, then small molecules were added and accelerated for transmembrane process. Integration time step was 1 fs, temperature was 298 K. Cutoff of 1.2 nm for nonbonding interactions, Ewald method for long-distance electrostatic interactions.

Study on the intestinal retention time of CLS

The residence time of CLS in the gastrointestinal tract was investigated by a small animal *in vivo* imager. Healthy Kunming mice weighing approximately 18–22 g were fasted for 12 h before the experiment. Cy5 NHS-labeled CLS was administered by gavage at a dose of 1 mg/kg, and the control group was given the same volume of normal saline. The mice were sacrificed at 0, 2, 4, 8, 12 and 24 h. The small intestine was dissected and removed. The contents were removed by gently swinging and washing with normal saline. After the excess water was removed by filter paper, a small animal *in vivo* imager was used for analysis.

Biodistribution of CLS in vivo

Retention in mice and their GI tract

The retention time of CLS in the gastrointestinal tract was investigated using a small animal *in vivo* imager. Healthy Kunming mice weighing approximately 18–22 g were fasted for 12 h before the experiment. Cy5.5-labeled CLS was administered by gavage at a dose of 1 mg/kg, and the control group was given the same volume of normal saline. Mice were sacrificed at 0, 2, 4, 8, 12 and 24 h, after which the small intestine was dissected. The contents were removed by gently shaking with normal saline, and the excess water was removed with filter paper and subsequently analyzed via a small animal living body imager. All animal experiments were performed in compliance with the relevant laws and institutional guidelines for the care and use of laboratory animals in China. The experiments were also reviewed and approved by the Ethical Review Committee and Laboratory Animal Welfare Committee of Shenyang Agricultural University, and the animal ethical approval number is 2023041002.

Retention in major organs and the intestinal villus

Following the operational steps and time points of active imaging, mouse intestinal tissue was taken and cross-sectional sectioning was performed. The tissue was stained with DAPI, and the uptake of Cy5.5-labeled CLS in the intestine was observed via CLSM. The heart, liver, spleen, lungs, and kidneys were also dissected and removed. The samples were washed with physiological saline, cleaned of residual blood, and placed on slides for observation in a live imaging device.

LC–MS determination of C3G distribution in major organs

Blood and organ tissues were collected at various time points (0 min, 5 min, 15 min, 30 min, 1 h, 2 h, 4 h, 8 h, 12 h, and 24 h). Tissue homogenate was centrifuged at 4000 rpm to obtain the supernatant, which was then treated with acetonitrile and acetone and centrifuged to remove precipitates. The resulting mixture was dried and a 1 mg/mL solution was prepared. LC-MS analysis was performed after passing the sample through an SPE column. The LC-MS analysis method can be found in the Supporting Information.

Animal experiments evaluating the effectiveness of nanosystems

Intervention effect on acute lung injury (ALI)

The groups and treatments of the rats (n = 8) are shown in Fig. 5. After the rats were euthanized, the lung organ indices and W/D ratios were recorded (left lung). The right lung of the rats was divided into two parts, with a portion fixed with 4 % paraformaldehyde and the other portion prepared as a single-cell suspension. Fixed lung tissue was subsequently tested for HE, Masson, IHC-P (NRF2), TUNEL, and ROS in the lung single-cell suspension. Part of the lung tissue was homogenized, the supernatant was collected, and the changes in cytokine content in the different intervention groups were measured using a reagent kit (for TNF-α, IL-1β, IL-6, IL-10, iNOS, COX-2, CAT, SOD, GSH and MDA).

Intervention effect on chronic lung injury (CLI)

The grouping and administration of the various treatments to the rats are shown in Fig. S17 (n = 8). The test indicators are basically consistent with those in section 2.14.1.

Intervention effect on LPS-induced colitis

The grouping and treatment of the rats are shown in Fig. S18 (n = 8). The rat colon and rectum were separated and photographed, with a portion fixed with 4 % paraformaldehyde and the other portion prepared as a single-cell suspension. The fixed colon was subsequently subjected to HE, Masson, IHC-P (Nrf2), TUNEL, and ROS staining. Part of the lung tissue was homogenized, the supernatant was collected, and the changes in cytokine content in the different intervention groups were measured using a reagent kit (for TNF-α, IL-1β, IL-6, IL-10, iNOS, COX-2, CAT, SOD, GSH and MDA).

Intervention effects on the gut microbiota

Three to five fecal samples were collected and stored at −80 °C before DNA extraction. The V3-V4 region of the bacterial 16S rRNA gene was amplified by PCR, purified, and quantified. The amplicons were mixed with barcodes, and the library was constructed for sequencing on the Illumina NovaSeq 6000 platform. Microbial diversity was analyzed. Fecal samples were mixed with water, centrifuged, and then added to a crotonate metaphosphate solution. After overnight incubation at −20 °C, the sample was centrifuged again before measurement using gas chromatography with a flame ionization detector.

Statistical analysis

The data are expressed as the means ± standard deviations (SD) and were subjected to one-way analysis of variance (ANOVA). All the statistical comparisons were performed via one-way ANOVA followed by Tukey's test using Origin 8.0 software. Differences were considered to be statistically significant when the *p* value was < 0.05.

Results

Characterization of CLS nanosystems

The prepared CLS and CL nanoparticles were characterized by TEM (Fig. 1). The particle size of CLS is approximately 30–40 nm, and the particle size of CL is approximately 40 nm. As can be seen from the AFM image (Fig. 1), CLS is a relatively uniform sphere with an average height of approximately 20–25 nm, and CL particles are also spherical with an average height of 30–50 nm. The TEM and AFM data are basically consistent. The nanosystem was dispersed into an aqueous solution, and the particle size of CLS was 88 nm (PDI = 0.122), while the particle size of CL was 98 nm (PDI = 0.133), indicating that the prepared CL and CLS had a uniform particle size distribution and good dispersion. The zeta potential of CLS and CL nanoparticles in different pH buffer solutions showed that the isoelectric point of CLS was approximately pH 4, close to the isoelectric point of SCN, while the isoelectric point of CL nanoparticles without SCN encapsulation was approximately pH 5.5. The above experimental results indicate that the surface of CLS nanoparticles is coated with SCN.

Particle size simulation of CLS nanosystems

Through calculations, it was found that the maximum diameter of the X/Y/Z space for phosphatidylcholine was ~10 Å/~24 Å/~17 Å, the maximum diameter of the X/Y/Z space for C3G was ~13 Å/~11 Å/~8 Å, the maximum diameter of the X/Y/Z space for casein was ~63 Å/~50 Å/~52 Å, and the maximum diameter of the X/Y/Z space for succinic acid was ~8 Å/~8 Å/~2 Å (Fig. 1H-J). The maximum spatial diameter of CLS was calculated as 24 Å+13 Å+63 Å+8 Å = 108 Å = 10.8 nm. Since the dry particle size of CLS was measured to be approximately 40 nm, the particle sizes of approximately four groups were the same after mixing and expanded to eight groups after hydration, and the possible self-assembly process and self-assembly molecular composition of CLS were inferred as shown in Fig. 1K.

Molecular dynamics analysis of self-assembly in nanosystems

The root mean square deviation (RMSD) of molecular dynamics (MD) simulation can reflect the motion process of the complex, with violent fluctuations indicating intense motion and vice versa indicating stable motion [30]. As shown in Fig. 2A-2C, in the SCN-Phosphatidylcholine-C3G complex, C3G exhibited the most stable fluctuations during the MD process, followed by the SCN-C3G complex. In the Phosphatidylcholine-C3G complex, both small molecules are unstable, indicating that the complex is unstable. The SCN-Phosphatidylcholine-C3G complex exhibited the most stable overall fluctuations in both small and protein macromolecules, indicating that CLS is the most stable.

In the SCN-C3G binary complex, C3G binds to the ATP pocket of the protein, which is flattened (Fig. 2A-2C) and can form hydrogen bonds with amino acids. However, due to the large opening of the pockets toward the solvent area, C3G may have a risk of being released from the pockets at any time. In the SCN-Phosphatidylcholine-C3G ternary complex, C3G is also bound to the ATP pocket. However, unlike the SCN-C3G binary complex, Phosphatidylcholine blocks the ATP pocket, preventing C3G from detaching from the pocket (Fig. 2D). In addition, C3G forms hydrogen bonds with more amino acids, such as VAL-116, ASP-175, ASN-161, and HIE-160, making their binding tighter. According to the energy values of the combined system (Table S2), the ternary composite system CLS has the lowest energy and is therefore the most stable.

CLS system element analysis and loading simulation

XPS is an effective method for detecting the type, chemical state, relative content and functional groups of elements on the surface of material [31]. XPS analysis (Table S3) revealed that the content of P element on CLS surface (0–8 nm) was 1.5 %. According to the experimental materials, all P comes from phosphatidylcholine, the main component of phosphatidylcholine (purity is 70 %), and the P content of phosphatidylcholine is 1.92 %. It can be concluded that the phosphatidylcholine distribution on the surface of CLSs is 1.5 %/ (1.92 %×70 %) = 54.7 %. That is, more than 50 % of the phospholipids in the CLS system were distributed within the

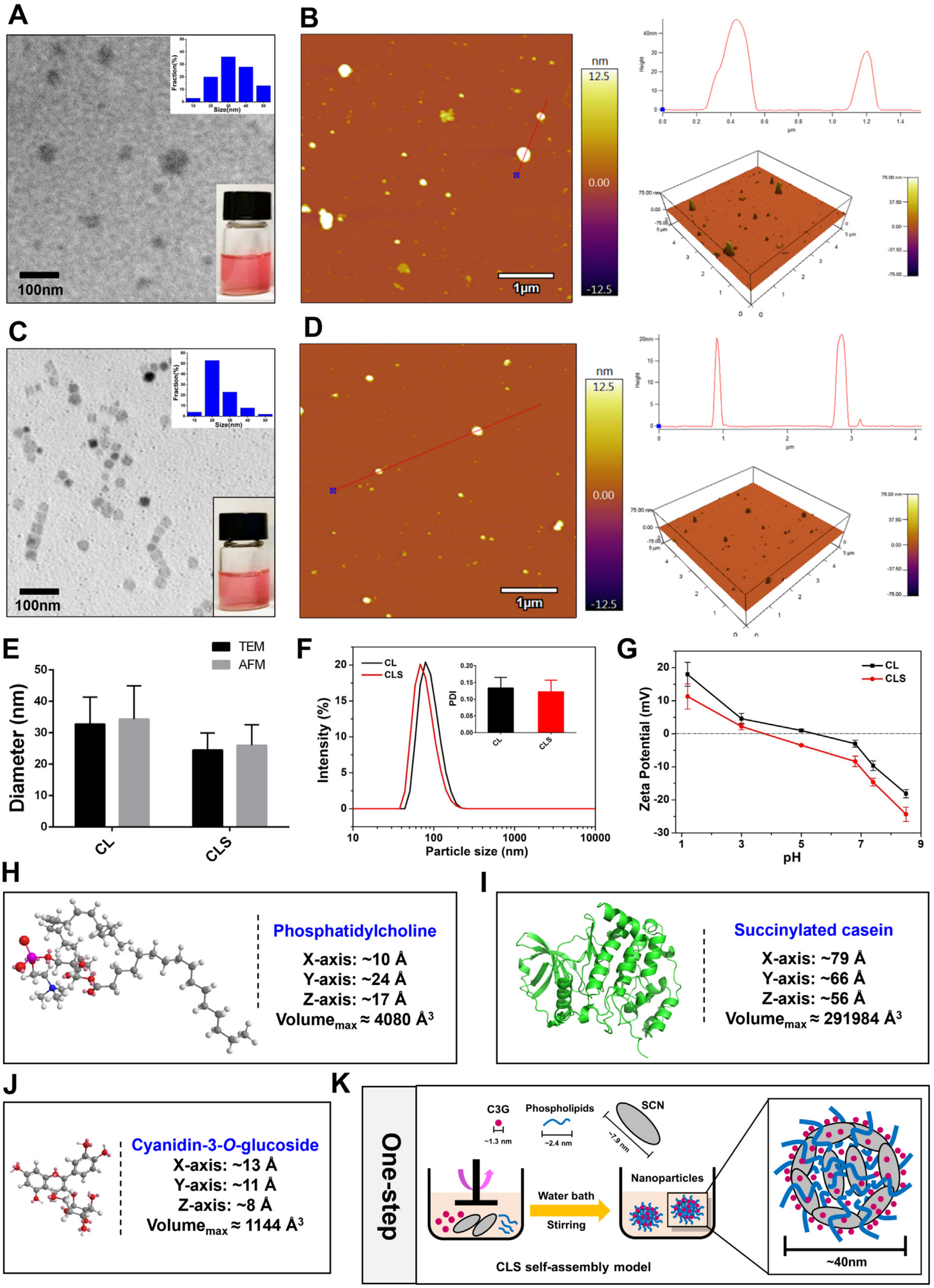

Fig. 1. Morphological characterization and particle size analysis of anthocyanin nanosystems. (A/C) TEM characterizations of CLS and CL nanocomposites. (B/D) AFM characterizations of CLS and CL nanocomposites. (E) The AFM, and TEM results of particle sizes of CL and CLS nanocomposites. (F) The size distribution and polydispersity (PDI) of CL and CLS nanocomposites. (G) The zeta potential of CL and CLS nanocomposites. (H-J) Material size calculation of nano-system. (K) Schematic diagram of preparation process and possible self-assembly simulation of CLS nanoparticles prepared by one-step method.

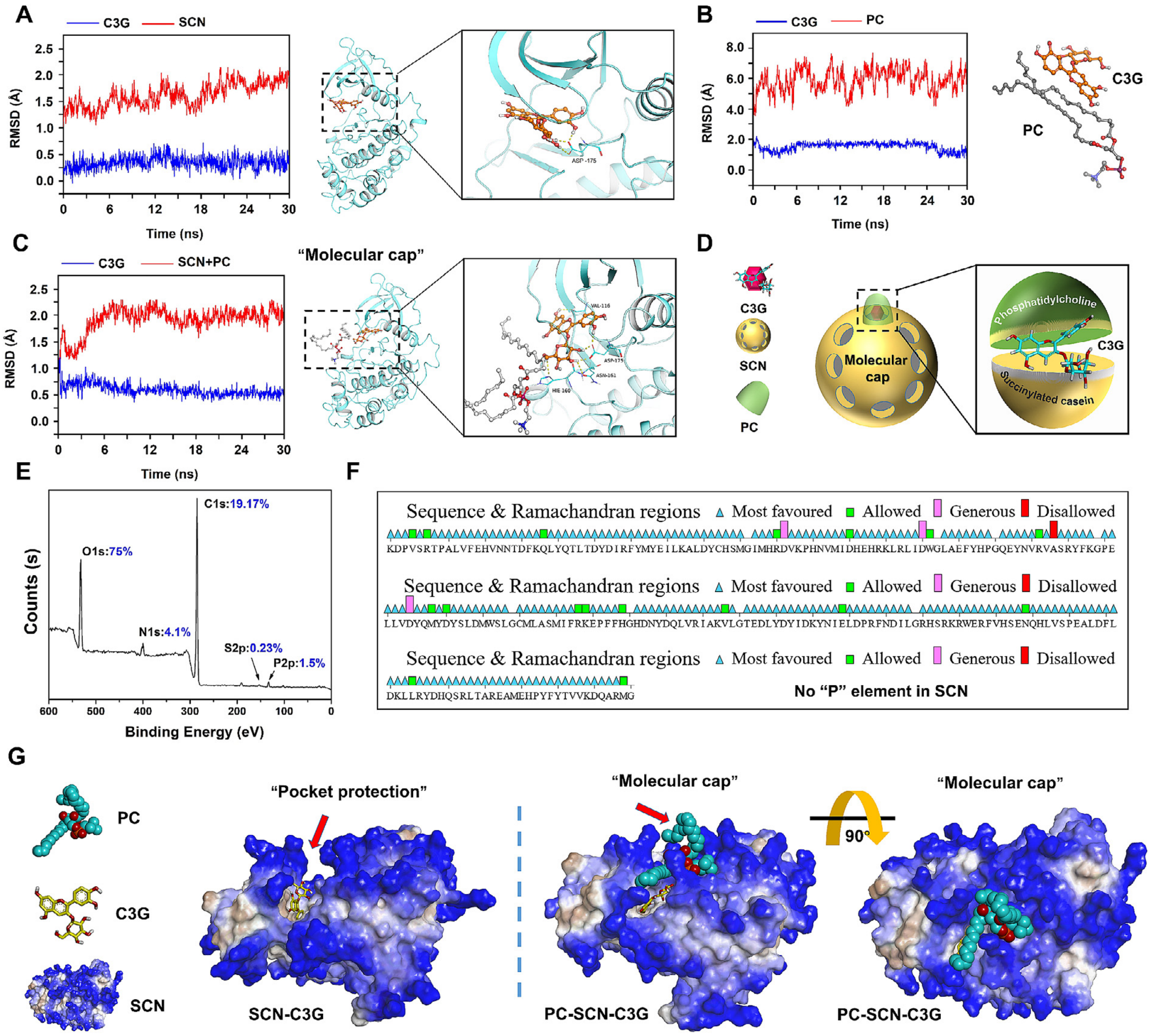

Fig. 2. Analysis and simulation of the protective effect of nano system on anthocyanins. (A-D) Schematic diagram of molecular dynamics analysis of CL and CLS nano-system formation. (E) Surface element analysis of CLS. (F) Amino acid sequence simulation analysis of SCN. (G) Schematic diagram of CLS forming "molecular cap" protection effect.

0–8 nm surface layer. The particle size of the CLS system is approximately 40 nm, which further proves that phospholipids are actively distributed in the outermost layer of the nanosystem and form a "molecular cap" protection phenomenon.

According to our molecular simulation (Fig. 2G), C3G is blocked by phosphatidylcholine in the outer region of the SCN. The blocking effect is mainly the H-bond effect, which is a strong interaction with 1.9 Å of LES-122 and 1.6 Å of HEE-160. Through this interaction, a structure similar to a cap is formed, which plays the protective role of a "molecular cap". According to the nanometer size predicted by quantum chemistry and the molecular mass ratio of the different molecules self-assembled, molecular dynamics were used to simulate the relative real state of self-assembly of the system. When the 500 ns system approached equilibrium, anthocyanins were distributed inside the protein, while phospholipids were more abundant on the outside, which further verified the possibility of the existence of a "molecular cap" (Fig. 2H). The electrostatic interactions between the negative SCN and the positively charged C3G, and the hydrophilic part of the phospholipid (polar part) through the hydrogen bond with the protein firmly, together to form a self-assembly system.

Characterization of the physicochemical parameters of the nanomaterials

Fig. 3 showed that C3G has a maximum absorption peak at 514 nm, while phospholipids and succinylated casein do not have absorption at this wavelength. This indicates that they do not interfere with the determination of anthocyanin content in the complex. CL (unmodified SCN) and CLS (modified SCN) have absorption peaks at 536 nm, confirming the successful encapsulation of anthocyanins. SCN exhibits endogenous fluorescence due to amino acid residues like tryptophan, tyrosine, and phenylalanine. Casein has a maximum fluorescence emission wavelength of around 345 nm, while C3G does not exhibit fluorescence. CLS nanoparticles show a small fluorescence emission peak at 330 nm, suggesting fluorescence quenching between casein and C3G (Fig. 3C). In terms of absorption peaks (Figure D), SCN has a peak at 202 nm, CL nanoparticles do not show a peak, and CLS nanoparticles have an absorption peak at approximately 202 nm. This indicates the successful preparation of CLS nanoparticles.

The encapsulation efficiency of CLS is between 9 % and 10 %, while the loading efficiency is approximately 60 % (Fig. 3E/3F).

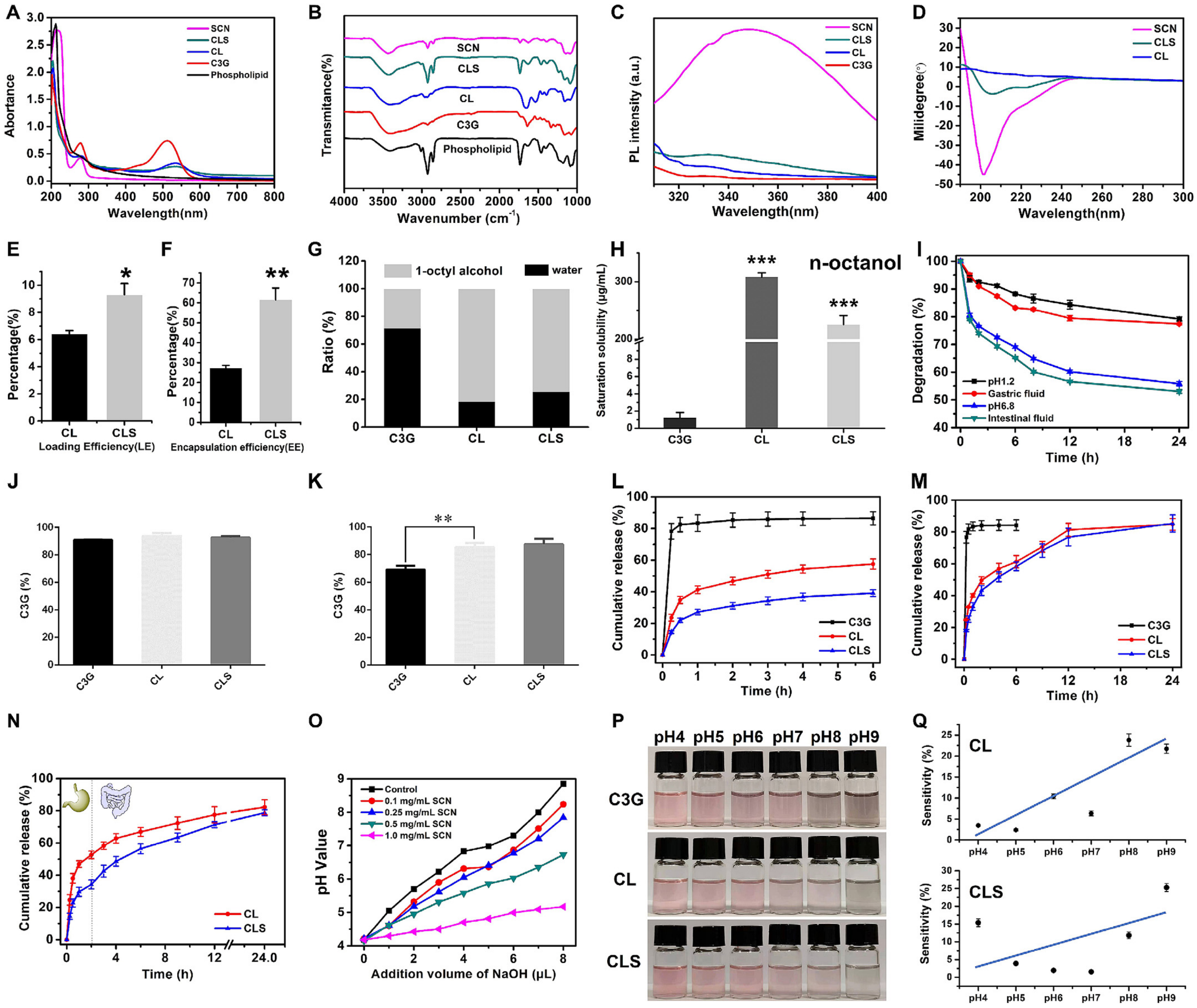

Fig. 3. Characteristic analysis of anthocyanin nano system. (A-D) UV/Vis absorbance spectra, FTIR spectra Fluorescence spectra and CD spectra of CL and CLS nanocomposites. (E) Loading efficiency (LE) of CL and CLS nanocomposites. (F) Encapsulation efficiency (EE) of CL and CLS nanocomposites. (G) Oil-water partition coefficient of CL and CLS nanocomposites. (H) Determination of saturated solubility of C3G, Cl and CLS in *n*-octanol. (I) Degradation curves of C3G in different media. Degradation curves of C3G, CL and CLS in simulated gastric fluids (J/L) and simulated intestinal fluids (K/M). (N) Release curves of C3G loaded by CL and CLS in simulated gastric-intestinal fluids. (O) Impact resistance of SCN materials to NaOH with different pH values. (P) Photos of C3G, CL and CLS nanocomposites solutions with different pH. (Q) Linear data of response of CL and CLS to different pH solutions. Data are presented as mean ± SD (n = 3). * $p < 0.05$, ** $p < 0.01$, ***$P < 0.001$.

These values are significantly higher than those of CL due to the negatively charged nature of the SCN polymer in CLS, which interacts with C3G to increase efficiency. The saturation solubility of C3G in *n*-octanol was 1.24 μg/mL, but with CLS nanoparticles it increased to 225 μg/mL, an increase of 182 times. Similarly, the saturation solubility of CL nanoparticles in *n*-octanol was 308 μg/mL, which was 248 times higher than that of free C3G (Fig. 3H). Both CL and CLS can greatly improve the solubility of C3G in *n*-octanol. The amphiphilicity of the CLS nanosystem was significantly changed compared to the C3G monomer, with increased lipid solubility achieved through the addition of phospholipids.

In vitro simulated digestion characteristics of CLS nanosystems

As shown in Fig. 3I-N, C3G showed good stability in simulated gastric juices, with a slight decrease in C3G, CL, and CLS contents after 2 h of incubation. C3G was reduced by approximately 35 % in simulated intestinal fluid, while CL and CLS significantly improved the stability of C3G. CLS exhibited a more pronounced sustained release effect, with less than 40 % C3G released at 6 h in simulated gastric juice. In simulated intestinal fluid, CLS showed cumulative release exceeding 80 % at 24 h, indicating relatively complete release of C3G.

Color changes in CLS nanosystems

Fig. 3O shows that as the amount of NaOH added gradually increases, the pH of the solution significantly increases, while the pH of the solution containing SCN does not change significantly. With increasing SCN concentration, the buffering ability of the solution became stronger, indicating that SCN has a certain buffering effect on the addition of NaOH.

As shown in Fig. 3P, the CLS and CL groups had a certain buffering effect on the amount of added NaOH, and the color change in the solution was not significant compared to that in the C3G group, while the CLS group had the smallest change. Further curve analysis of the RGB values of the colors showed that CLS had a smoother slope and better resistance to color changes (Fig. 3Q).

Cell uptake of the CLS nanosystem

The experimental results demonstrated (Fig. 4A) that there was no CLS green fluorescence in the control group, but weak green fluorescence was observed in Caco-2 cells incubated with CLS for 0.5 h. The green fluorescence inside the cells increased with longer incubation times, indicating a time-dependent uptake of CLS by Caco-2 cells. Flow cytometry analysis showed (Fig. 4B/C) that cellular intake of anthocyanins significantly increased as the incubation time increased from 0.5 h to 4 h, particularly at 2 and 4 h. Molecular simulation methods were used to assess the absorption ability of CLS in cells. The results indicated that the interaction energy between CLS and the phospholipid bilayer decreased gradually, while C3G maintained a consistent energy level. This suggests that CLS has better membrane permeability than C3G, supporting the superior cellular absorption ability of CLS (Fig. 4D). Cytotoxicity assays (Fig. S9-S11) demonstrated that CLS exhibited no adverse effects on Caco-2 or HepG2 cells, even at high concentrations (50 μg/mL). CLS also enhanced cell viability under oxidative stress, confirming its biocompatibility.

In vivo absorption of the CLS nanosystem in mice

After 2 h of oral administration, CLS was distributed throughout the entire intestinal segment, with a higher proportion in the upper part of the intestine. By 4 h, CLS was evenly distributed throughout the entire intestinal segment, reaching its maximum relative fluorescence intensity. From 8 h onwards, the fluorescence intensity in the intestine began to decrease, with weak signals still detectable at 24 h (Fig. 4E). These experiments demonstrate that CLS has strong retention in the intestine, with a retention time exceeding 12 h, facilitating uptake by small intestine tissue. Cy5.5-labeled CLS showed strong fluorescence signals in the duodenum, jejunum, and ileum, with the highest absorption in the ileum. The time for maximum intestinal fluorescence intensity was consistent with *in vivo* imaging data (Fig. 4F).

Targeted enrichment of CLSs in the lung

As shown in Fig. 4G, after oral administration of Cy5.5-labeled CLS, it is significantly distributed in the lungs and weakly distributed in the liver (the main metabolic organ of anthocyanins). The main distribution time in the liver was between 2 and 8 h, while it was distributed in the lungs between 2 and 24 h, especially in the 2–12 h range. It can be preliminarily inferred that the nanosystem has a good lung distribution effect and exhibits a lung-targeting effect.

Further LC-MS was used to detect the distribution of CLS *in vivo* tissues. The concentration distribution of C3G in the lungs was consistent with the trend observed via fluorescence imaging (Fig. S15 and Fig. 4H), in which C3G was significantly enriched after 2–8 h ($P < 0.01$), while the concentration of the C3G monomer was almost zero. This phenomenon suggested that the carrier delivered C3G to the lungs and produced a significant targeted enrichment effect. Comparing and analyzing other major organs (Fig. S15), although the C3G concentration in the CLS system slightly increased, there was no sudden increase, as in the lung tissue. Compared to that of C3G, the lung C_{max} of CLS was 4.7 times higher, the $AUC_{(0\text{-}t)}$ was 25.7 times higher, and the $T_{1/2}$ was extended from 0.321 h to 1.174 h.

Sustained release effect of CLS on the intestinal tract

After inducing colitis with LPS (Fig. S18C), the rats' intestinal length was significantly shortened by about 20–25 % compared to the control group ($P < 0.05$). Treatment with C3G and CLS showed improvement, with the CLS group having the best effect, reducing the shortening to approximately 5 % ($P < 0.01$ vs model group). SCNCL treatment did not have a significant effect on intestinal length ($P > 0.05$ vs model group). HE and Mason morphological analysis revealed that the enteritis model group exhibited typical features of intestinal damage, inflammatory infiltration, and tissue fragmentation (Fig. S18D). Treatment with C3G showed a trend toward recovery, while CLS had the mildest inflammatory characteristics. Nrf2 expression in the colitis model group was significantly increased ($P < 0.001$ vs control group), but decreased after treatment, with CLS showing the most significant downregulation ($P < 0.01$ vs model group) (Fig. S18).

As shown in Fig. S18D and G, compared to the blank group, the enteritis group showed a significant increase in apoptosis rate ($P < 0.001$), with a rise from 3 % to 23 %. After treatment, C3G (14.4 %, $P < 0.01$ vs model group), SCN + CL (14.7 %, $P < 0.01$ vs model group), and CLS (7.1 %, $P < 0.001$ vs model group) all led to a decrease in apoptosis, with CLS showing the most significant effect.

ROS analysis (Fig. S18E/5H) revealed that ROS levels were significantly higher in the enteritis group compared to the blank group ($P < 0.001$ vs model group). Treatment with C3G ($P < 0.01$ vs model group) and CLS ($P < 0.001$ vs model group) resulted in a decrease in ROS levels, with CLS showing the most significant effect.

CLS had better regulatory effects on inflammatory factors TNF-α, IL-1β, IL-6, IL-10, iNOS, and COX-2 compared to C3G and SCNCL (Fig. S18I/R). CLS also showed better regulation of oxidative stress-related enzymes CAT, SOD, GSH, and MDA overall, indicating its superior ability to resist oxidative damage compared to C3G and SCNCL (Fig. S18).

Effect of sustained release of CLSs on the gut microbiota

Pielou, Shannon, and Simpson diversity analyses in Fig. S19 showed significant changes in microbial diversity in colitis model rats. The CLS group had a more diverse microbial community compared to the control group, while the C3G group was similar to the control group. The SCNCL group had particularly significant differences. C3G was found to improve intestinal diversity in inflammatory models, with enhanced effects after nanodelivery. The Venn plot in Fig. S19D/F displayed 1186 common OTUs among the five groups, with the control group having the most unique OTU species. PCA indicated a significant difference in gut microbiota between the model group and other groups. The CLS and SCNCL groups showed similar results to the model group, suggesting that CLS can improve intestinal microbiota and return it to normal levels effectively.

The abundance of Firmicutes in the gut microbiota of the MOD group significantly increased, while the relative abundance of Bacteroidetes decreased (Fig. S19G/I). The proportion of Firmicutes/Bacteroidetes in the MOD group significantly increased compared to the blank group. CLS reduced the relative abundance of Firmicutes and increased the relative abundance of Bacteroidetes, reversing the increase in the Firmicutes/Bacteroidetes ratio. Changes in the abundances of Firmicutes, Bacteroidetes, Actinobacteria, and other phyla in each group were not dose dependent, indicating a complex system in the gut microbiota. The

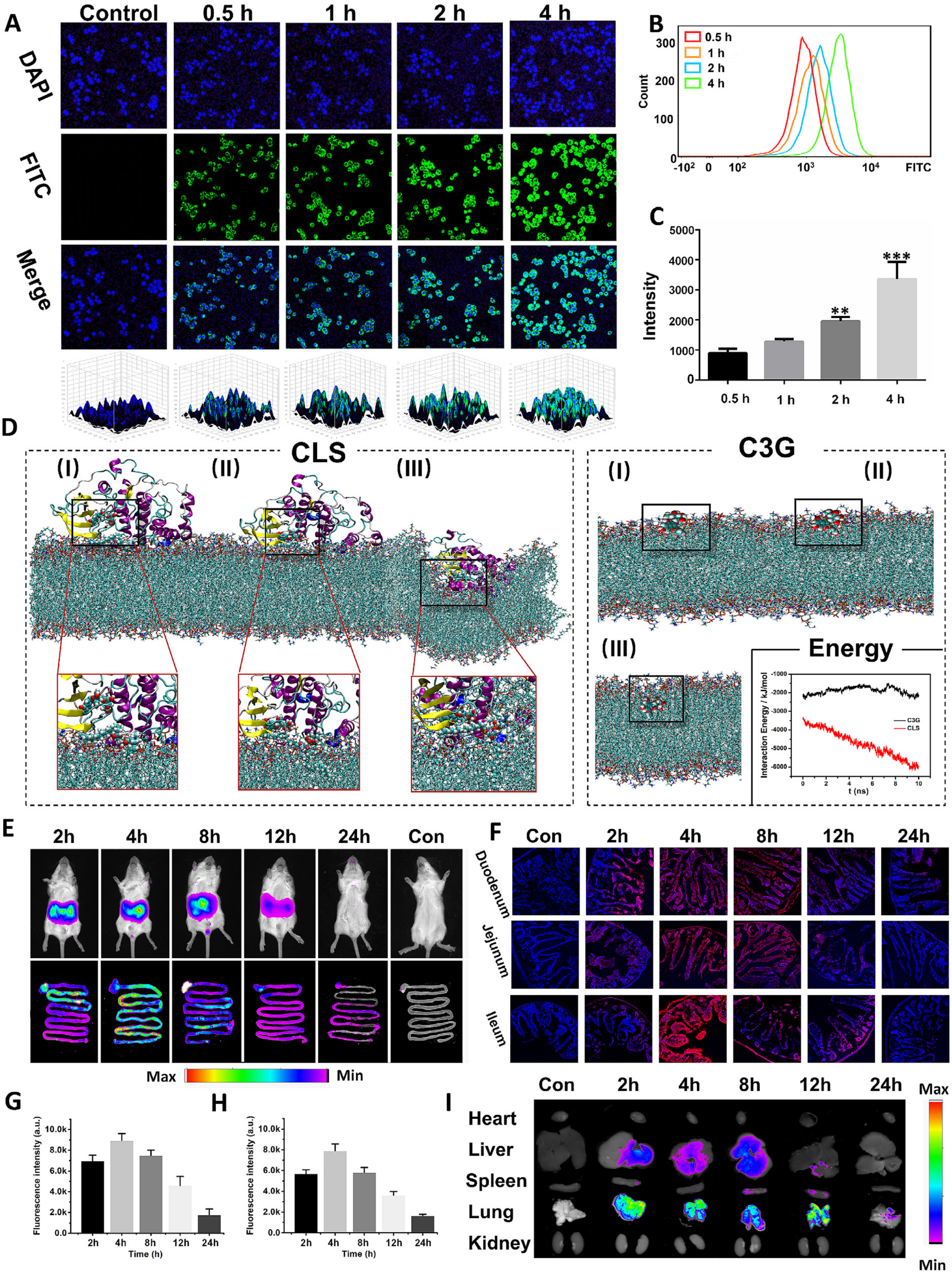

Fig. 4. Absorption and sustained release of CLS in cells and mice. (A) CLSM images of cellular uptake of FITC-labelled CLS incubation with Caco-2 cells. (B) MFI of CLS in Caco-2 cells was measured by FACS. (C) Fluorescence intensity analysis from part B. (D) Molecular Dynamics Study of CLS and C3G Permeable Membrane. (E/G) Biodistribution of CLS: the mice were orally administered with CLS, and the fluorescence images of the gastrointestinal tract were obtained at various time points (2, 4, 8, 12, 24, and control). (F/H) The absorption and distribution effect of CLS in the intestinal wall of mice. (I) The distribution of CLS in organs of mice at different time points (2, 4, 8, 12, 24, and control). Data are expressed as mean ± SD (n = 3). $^{**}P < 0.01$, $^{***}P < 0.001$ vs 0.5 h group.

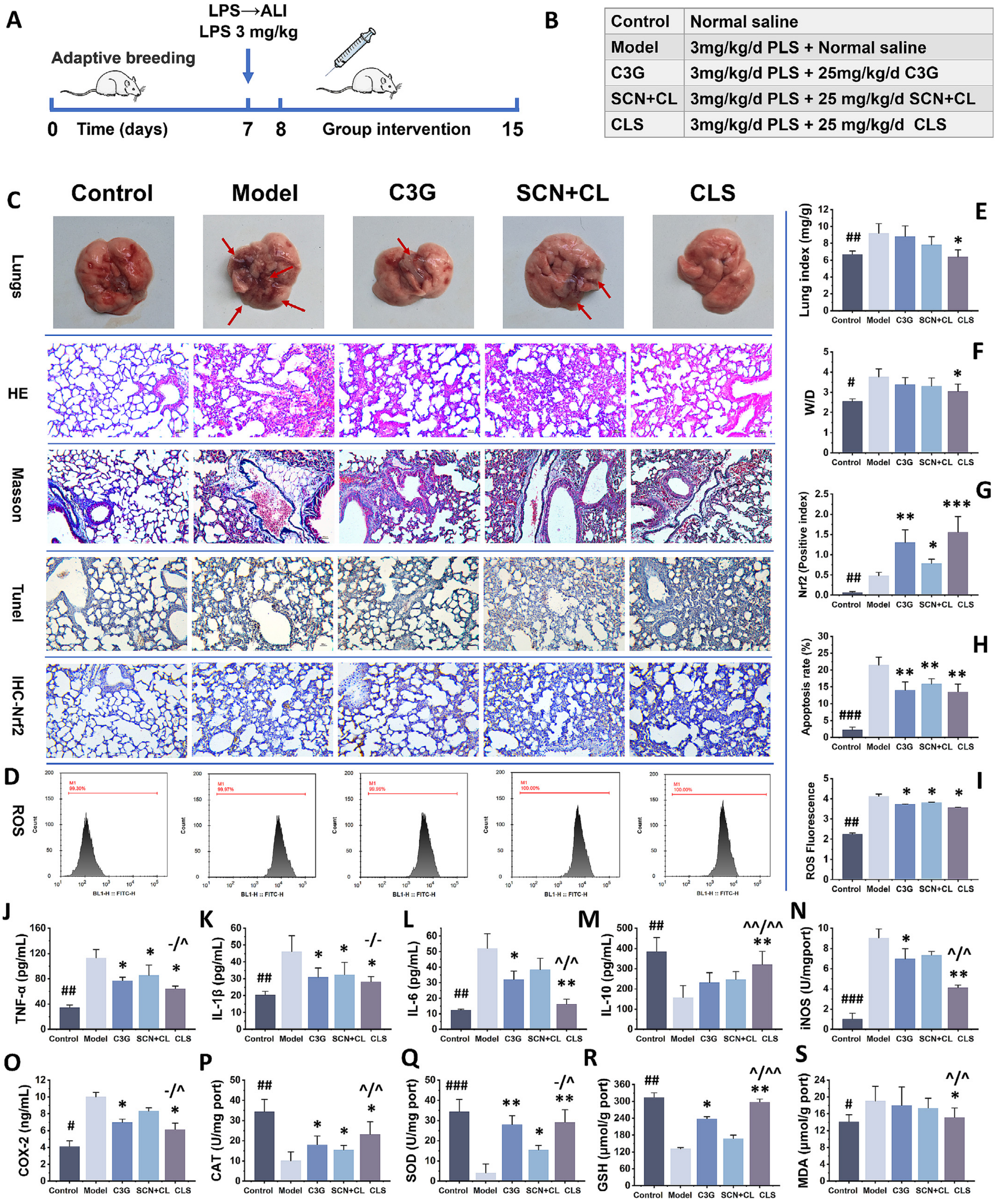

Control	Normal saline
Model	3mg/kg/d PLS + Normal saline
C3G	3mg/kg/d PLS + 25mg/kg/d C3G
SCN+CL	3mg/kg/d PLS + 25 mg/kg/d SCN+CL
CLS	3mg/kg/d PLS + 25 mg/kg/d CLS

Fig. 5. Interventional effect of CLS on acute lung injury (ALI). Animal experiment plan (A) and dosage (B); Cross sectional morphology of colon (Lungs, HE, Masson and Tunel) (C); Change in ROS expression level (D); Changes in physiological indicators (Lung index, W/D, Nrf2, apoptosis rate, ROS, TNF-α, IL-1β, IL-6, IL-10, iNOS, COX-2, CAT, SOD, GSH and MDA) (E-S). *$P < 0.05$, **$P < 0.01$, ***$P < 0.001$ vs Model group.

results of the genus-level composition and abundance analyses (Fig. S19H) showed that Prevotella_9 and Prevotella_1 were two relatively abundant bacterial genera in the five groups. Prevotella_1 was enriched in SCNSL, while Prevotella_9 was highly abundant in the other four groups. Fecal short-chain fatty acid (SCFA) content in the mice changed significantly in the different intervention groups, with total fatty acid content and acetic acid, propionic acid, and butyric acid content decreasing after inflammation induction and increasing significantly after interventions, especially in the CLS group (Fig. S19J–M).

The alleviating effect of CLS on lung injury

After inducing acute lung injury (ALI) in mice, significant lung damage such as necrotic tissue and plaque-like tissue was observed, indicating successful modeling (Fig. 5C). Following intervention with C3G, SCNCL, or CLS, there was a significant improvement in lung morphology with a decrease in the number of necrotic plaques, particularly in the CLS group. Analysis of lung organ indices and lung wet/dry ratios (Fig. 5E/F) showed that the ALI group had a significant increase compared to the blank control group. Only the CLS group exhibited a downward trend after intervention, suggesting that CLS had a mitigating effect on ALI. Morphological analysis revealed (Fig. 5C-HE/Mason) inflammatory features in the ALI group, including alveolar wall thickening, red blood cells, inflammatory cell infiltration, and alveolar fragmentation. The SCNCL group showed no significant change, the C3G group showed some recovery, and the CLS group had the mildest inflammatory characteristics.

Significant apoptosis was observed in the ALI group compared to the blank group ($P < 0.001$) (Fig. 5C-TUNEL/H). After treatment, the apoptosis of C3G, SCNCL, and CLS all decreased significantly ($P < 0.01$), indicating that these three agents had protective effects on the lungs. The expression of Nrf2 (Fig. 5C-Nrf2/5G) in the lung tissue of the ALI group was significantly increased compared to the control group ($P < 0.01$). After treatment, the expression of Nrf2 further increased, with CLS showing the most significant upregulation ($P < 0.001$). ROS analysis showed (Fig. 5D/5I) that the ALI group had a significant increase in ROS compared to the blank group ($P < 0.01$), while different intervention groups were downregulated ($P < 0.01$) after treatment. The CLS group exhibited greater regulation of inflammatory cytokines (Fig. 5J–P) and oxidative stress-related enzymes (Fig. 5Q–S) compared to the C3G and SCNCL groups, indicating that CLS has a better ability to prevent oxidative damage in ALI.

After inducing chronic lung injury in rats, the lungs showed visible damage such as necrotic tissue and plaques, confirming successful modeling (Fig. S17C). Treatment with C3G, SCNCL, and CLS significantly improved lung morphology and reduced necrotic plaques, with the CLS group showing the most improvement. Organ indices and lung wet-dry ratio were significantly higher in the CLI group compared to the control group, but only the CLS group showed a decrease after intervention, indicating that CLS had a beneficial effect on chronic lung injury (Fig. S17E/S17F).

Morphological analysis showed (Fig. S17C-HE/Mason) that the CLI group had signs of pneumonia. After treatment, there was no significant change in the SCNCL group; the C3G group showed a recovery trend, and CLS had the lightest inflammatory characteristics. Immunohistochemical analysis of Nrf2 revealed (Fig. S17C-Nrf2/S17G) that the expression of Nrf2 was significantly increased in the CLI group, with CLS showing the most significant regulatory effect. Apoptosis was significantly observed in the CLI group (Fig. S17C-TUNEL/S17H), but decreased after intervention in all groups, with CLS showing the most protective effect on stem cells. ROS analysis showed that ROS levels (Fig. S17C-ROS/S17I) were significantly increased in the CLI group, but decreased in the C3G and CLS groups after intervention. CLS was more effective than C3G or SCNCL in preventing oxidative stress and apoptosis in CLI induced by LPS. CLS also had better regulatory effects on inflammatory cytokines (Fig. S17J-P) and oxidative stress-related enzymes (Fig. S17Q-T) compared to C3G and SCNCL.

The regulatory effect of CLS on the lung-gut axis

The levels of HGF, IL-17, IL-22, IL-1β, IL-6 and IL-10 in the lung and HGF, VIP, IL-17, IL-22, SCFA, IL-1β, IL-6 and IL-10 in the intestine of chronic lung injury model rats were tested (Fig. S16). The results showed that the lung and gut can establish obvious lung-gut interactions through immune factors and gut microbiome secreted factors.

Discussion

Anthocyanins have been known for over a century [32] for their pigment properties [33] and have been studied for their effects on plants [34], as well as their nutritional and health benefits [5–11]. However, anthocyanins have two major drawbacks: structural instability and low bioavailability [1,26,35]. The flavylium cation in the anthocyanin structure is prone to reactions that can lead to instability, while its high polarity makes it difficult for the body to absorb. Researchers have focused on protecting the C-ring of anthocyanins to improve their stability and absorption through various methods such as self-assembly of multi-anthocyanin molecules, metal chelation, small-molecule conjugation (sandwich), and macromolecular wrapping (hand-glove) [34].

This research also follows the basic principles of the above design. Based on our research team's previous application of the "hand-glove" principle to embed anthocyanins in casein, we further designed a "molecular cap" anthocyanin nano-protection system. The main advancement of this system is that (I) the protein is acylated to form a pocket center negative pocket cavity, which can form local electrostatic interactions with positively charged anthocyanin molecules (ionic bond, bond energy of 20–40 kJ/mol) [36]. The protective effect of this approach is more obvious than that of conventional protein encapsulation, which mainly relies on van der Waals forces (bond energy of 0.3–1.9 kJ/mol) and hydrophobic interactions (bond energy of 3–4 kJ/mol) [37]. However, to allow more anthocyanins to be absorbed in the small intestine after multiple digestive tract ingestions, (II) we coated phospholipids on the outside through hydrogen bonding and purposefully designed an anthocyanin-specific protection system with succinylated casein as the embedded skeleton and phospholipids as the outer "molecular cap". (III) Importantly, the whole design of the nanosystem in this study was completed under the guidance of computational chemistry, from the selection of raw materials to the design of the "molecular cap" system and subsequent measurement of nanoparticle size.

This study successfully used multidimensional computational chemistry simulation, including quantum computational chemistry, molecular docking, and molecular dynamics, to design anthocyanin nanosystems for food applications. This approach provides a valuable reference for designing other active food small molecule systems in the future. While molecular simulation has been used in the past for designing food active molecules, such as using molecular docking to study interactions between small and large molecules [23], and molecular dynamics to simulate self-assembly processes [22], there have been few successful cases of applying multidimensional molecular simulation to experimental design in the food industry. In the past, simulations were mainly used for verification purposes, with results compared to experiments to provide explanations [23,24]. However, deep multidimensional simulation often failed to fully match experimental results, leading to interpretation challenges. As a result, food system design has traditionally relied more on empirical and semiempirical rules [20,21]. With advancements in models and algorithms, there is potential for molecular simulation to be more widely used in food system design, similar to how computer-aided drug design has been successful [38]. The high level of agreement between multidimensional simulation and food chemistry experiments in this study suggests that computer-aided food design could be a promising research direction in the future.

The CLS hydrated particle size was determined to be 88 nm with a PDI of 0.122, while achieving an encapsulation efficiency of 62.1 % and a loading efficiency of 10.2 %. Notably, it exhibits good biocompatibility and color stability. The choice of CLS carrier materials takes into account food sources and delivers exceptional nanoperformance. The process optimization findings from this study highlight a one-step self-assembly method that offers valuable applications.

The CLS system with "molecular cap" protection was shown to improve the bioavailability of anthocyanins with a significant sustained release effect in a study using four dimensions of *in vitro* simulated digestion, cellular uptake, animal uptake, and computational simulation. The CLS system demonstrated a long-term sustained release effect of 24 h. Pharmacokinetic analysis revealed that, compared to that of C3G, the C_{max} in the blood of CLS was 2.5 times that of C3G, and the $AUC_{(0-t)}$ was 13.1 times that of C3G. $T_{1/2}$ was extended from 0.426 h to 2.052 h. The improvement in pharmacokinetic parameters was revolutionary. According to our literature review, the corn alcohol-soluble protein-anthocyanin complex increased the blood AUC to 4.8 times that of free anthocyanins, and the α –lactalbumin nanotube system increased the blood AUC to 7.3 times that of free drugs, there have been no reports of an increase of more than 10 times in the $AUC_{(0-t)}$ of anthocyanins [14,39–41]. This study has used the dual optimization of anthocyanin stability and absorption efficiency by molecular cap design, as well as the breakthrough of the intestinal barrier by charge regulation, which has greatly increased the $AUC_{(0-t)}$ of anthocyanins by approximately 13 times, solving the long-standing problem of the low oral bioavailability of anthocyanins, which is a great milestone.

Oral targeting is a noninvasive drug delivery strategy for achieving systematic or remote targeting through oral routes and has the advantages of convenient administration and high compliance [42,43]. To achieve oral targeting, breakthroughs are needed: (I) a highly acidic stomach environment, (II) an intestinal barrier and microbial degradation, and (III) enrichment of target organs [44,45]. These three major biological barriers greatly reduce the possibility of oral targeting and necessitate strict requirements for the design of oral drug delivery systems. At present, the design of targeted delivery molecules is based mainly on intravascular administration because this mode of administration can eliminate the above drawbacks and provide better bioavailability and targeting [46,47]. However, when anthocyanins are used as food raw materials, the application scenario cannot be designed for intravascular administration modes such as drugs; additionally, the more likely direction is to be developed as precision nutritional food, and oral absorption is easy to accept by the public. At present, studies on the oral targeting of anthocyanins have gradually become popular [48–50]. However, due to the many biological barrier effects of oral administration, the targeting of anthocyanins is mainly reflected in the intestine, especially in colitis [51,52], and there are no clear oral targeting studies on organs. Molecular prototypes of anthocyanins have been shown to have clear effects on lung health, such as inhibiting the proliferation of lung cancer [53], improving PM10-induced lung damage [54], resisting radiation lung damage [55], and treating pulmonary hypertension and fungal pneumonia [56]. The CLS designed in this study realized the oral pulmonary targeting effect of anthocyanins for the first time, and the lung bioavailability increased by more than 20 times, which could further enhance the lung treatment and health care efficacy of anthocyanins. At present, targeted molecular delivery design mainly focuses on targeting disease sites because of the following clear targeting design principle: factors triggering corresponding [19], specific recognition, etc. These targeting designs are more suitable for drug design. Nondisease targeting is often more difficult because it does not provide clear lesion identification information, but nondisease targeting is more suitable for the health care design principle of food, targeted health protection in the early stage of disease, a healthier diet, and accurate nutritional information. However, the CLS nanoparticles we designed exhibit significant targeting effects in non-disease states. The lung-targeting capability of the CLS nanosystem in non-disease states likely arises from a synergistic interplay of its structural and physicochemical properties. First, the nanoscale size (~88 nm) and uniform spherical morphology enable passive targeting by evading rapid clearance mechanisms, prolonging systemic circulation, and facilitating accumulation in lung tissues [18]. Second, the negatively charged surface, conferred by succinylated casein, reduces nonspecific interactions with gastrointestinal mucus while potentially promoting electrostatic affinity for lung endothelial cells or surfactant-associated receptors. Third, the succinyl groups introduced through casein modification not only enhance hydrophilicity and anthocyanin encapsulation but may mimic endogenous ligands, enabling selective binding to lung-specific biomolecules. Finally, the phospholipid "molecular cap" stabilizes the nanosystem through hydrogen bonding and hydrophobic interactions, while its resemblance to pulmonary surfactant components could drive preferential localization in lung tissues [57]. Together, these features: nanoscale design, surface charge modulation, molecular mimicry, and lipid-mediated stealth properties, collectively underpin the observed lung-targeting efficacy of CLS.

The CLS nanosystem designed in this study not only has a lung-targeting effect but also has a lung-targeting effect [58] under non-disease conditions. This is the first report on the design of an organ-targeting nanosystem for oral anthocyanins in a non-disease state, which is important for the absorption and nutrient delivery of anthocyanins *in vivo*. Unfortunately, the mechanism of lung targeting in non-disease states is challenging to verify, unlike disease targeting. Future work we should prioritize interdisciplinary approaches combining computational modeling, *in vivo* imaging, and molecular biology to unlock the full potential of this innovative platform.

Conclusion

In this study, based on the guidance of multidimensional computational chemistry, a phospholipid-succinylated casein-anthocyanin nanosystem CLS with "molecular cap" protection was constructed by a one-step self-assembly method. The nanosystem CLS has good nanoscale properties and good stability and biocompatibility potential. This CLS is the first to achieve oral targeting of anthocyanins-lung targeting, with lung bioavailability increased by over 25 times and blood bioavailability increased by over 13 times. It also demonstrated a significant *in vivo* sustained-release effect of more than 24 h, showing a therapeutic impact on lung and intestinal diseases through the "lung-gut" axis. This study provides a new perspective and a feasible scheme for the nutritional application of anthocyanins.

Compliance with ethics requirements

All animal experiments were performed in compliance with the relevant laws and institutional guidelines for the care and use of laboratory animals in China. The experiments were also reviewed and approved by the Ethical Review Committee and Laboratory Animal Welfare Committee of Shenyang Agricultural University, and the animal ethical approval number is 2023041002.

CRediT authorship contribution statement

Jin-Long Tian: Writing – review & editing, Writing – original draft, Conceptualization. **Nuo Wang:** Validation. **Qin-Fu Zhao:** Visualization. **Zhi-Huan Zang:** Software. **Zhi-Ying Li:** Software. **Zhen-Yu Wang:** Supervision. **Ying Zhou:** Supervision. **Bao-Ru Yang:** Supervision. **Sergey S. Makarov:** Visualization. **Anton I. Chudetsky:** Visualization. **Liang Wang:** Resources. **Ying He:** Resources. **Bin Li:** Funding acquisition.

Declaration of competing interest

The authors declare that they have no known competing financial interests or personal relationships that could have appeared to influence the work reported in this paper.

Acknowledgments

This work was supported by the Natural Science Foundation of China (32202074 and U21A20273), the National Key R&D Program of China (2024YFD1600604), the Xingliao Talent Plan of Liaoning Province (XLYC2202023), the Key Research and Development Program of Liaoning Province (2024JH2/102500065), the Lingyan Project of Zhejiang Province (2023C02046), and the Scientific Research Foundation of Shenyang Agricultural University (880418027).

Appendix A. Supplementary data

Supplementary data to this article can be found online at https://doi.org/10.1016/j.jare.2025.05.059.

References

[1] Cruz L, Basílio N, Mateus N, de Freitas V, Pina F. Natural and synthetic flavylium-based dyes: the chemistry behind the color. Chem Rev 2021. doi: https://doi.org/10.1021/acs.chemrev.1c00399.

[2] Nalbant SS, Steacy S, Sieh K, Natawidjaja D, McCloskey J. Earthquake risk on the Sunda trench. Nat 2005. doi: https://doi.org/10.1038/nature435756a.

[3] Ding N, Zhou Y, Dou P, Feng R, Hong H, Luo Y, et al. Colorful and nutritious abundance: potential of natural pigment application in aquatic products. Food Innov Adv 2024. doi: https://doi.org/10.48130/fia-0024-0023.

[4] Denish PR, Fenger J-A, Powers R, Sigurdson GT, Grisanti L, Guggenheim KG, et al. Discovery of a natural cyan blue: a unique food-sourced anthocyanin could replace synthetic brilliant blue. Sci Adv 2021. doi: https://doi.org/10.1126/sci adv. abe7871.

[5] Solomon A, Golubowicz S, Yablowicz Z, Bergman M, Grossman S, Altman A, et al. EPR studies of $O_2^{\bullet-}$, OH, and $^1O_2$ scavenging and prevention of glutathione depletion in fibroblast cells by cyanidin-3-rhamnoglucoside isolated from fig (Ficus carica L.) fruits. J Agr Food Chem 2010. doi: https://doi.org/10.1021/jf100153z.

[6] Lin J, Tian J, Shu C, Cheng Z, Liu Y, Wang W, et al. Malvidin-3-galactoside from blueberry suppresses the growth and metastasis potential of hepatocellular carcinoma cell Huh-7 by regulating apoptosis and metastases pathways. Food Sci Hum Wellness 2020. doi: https://doi.org/10.1016/j.fshw.2020.02.004.

[7] Sun H, Mu T, Liu X, Zhang M, Chen J. Purple sweet potato (*Ipomoea batatas L.*) anthocyanins: preventive effect on acute and subacute alcoholic liver damage and dealcoholic effect. J Agr Food Chem 2014. doi: https://doi.org/10.1021/jf405032f.

[8] Chen P-N, Chu S-C, Chiou H-L, Kuo W-H, Chiang C-L, Hsieh Y-S. Mulberry anthocyanins, cyanidin 3-rutinoside and cyanidin 3-glucoside, exhibited an inhibitory effect on the migration and invasion of a human lung cancer cell line. Cancer Lett 2006. doi: https://doi.org/10.1016/j.canlet.2005.04.033.

[9] Tian J-L, Si X, Wang Y-H, Gong E-S, Xie X, Zhang Y, et al. Bioactive flavonoids from *Rubus corchorifolius* inhibit α-glucosidase and α-amylase to improve postprandial hyperglycemia. Food Chem 2021. doi: https://doi.org/10.1016/j.foodchem.2020.128149.

[10] Yao N, Lan F, He R-R, Kurihara H. Protective effects of bilberry (*Vaccinium myrtillus L.*) extract against endotoxin-induced uveitis in mice. J Agr Food Chem 2010. doi: https://doi.org/10.1021/jf904572a.

[11] Suresh S, Begum RF, Singh SAVC. Anthocyanin as a therapeutic in Alzheimer's disease: a systematic review of preclinical evidences. Ageing Res Rev 2022. doi: https://doi.org/10.1016/j.arr.2022.101595.

[12] Yeh T-S, Yuan C, Ascherio A, Rosner BA, Willett WC, Blacker D. Long-term dietary flavonoid intake and subjective cognitive decline in US men and women. Neurology 2021. doi: https://doi.org/10.1212/WNL.0000000000012454.

[13] Kent K, Charlton KE, Netzel M, Fanning K. Food-based anthocyanin intake and cognitive outcomes in human intervention trials: a systematic review. J Hum Nutr Diet 2016. doi: https://doi.org/10.1111/jhn.12431.

[14] Lang Y, Tian J, Meng X, Si X, Tan H, Wang Y, et al. Effects of α-casein on the absorption of blueberry anthocyanins and metabolites in rat plasma based on pharmacokinetic analysis. J Agr Food Chem 2021. doi: https://doi.org/10.1021/acs.jafc.1c00082.

[15] Gui H, Sun L, Liu R, Si X, Li D, Wang Y, et al. Current knowledge of anthocyanin metabolism in the digestive tract: absorption, distribution, degradation, and interconversion. Crit Rev Food Sci 2022. doi: https://doi.org/10.1080/10408398.2022.2026291.

[16] Lila MA, Burton-Freeman B, Grace M, Kalt W. Unraveling anthocyanin bioavailability for human health. Annu Rev Food Sci T 2016. doi: https://doi.org/10.1146/annurev-food-041715-033346.

[17] Li Z, Wang Y, Song B, Li J, Bao Y, Jiang Q, et al. The comparison between zein-anthocyanins complex and nanoparticle systems: stability enhancement, interaction mechanism, and in silico approaches. Food Chem 2023. doi: https://doi.org/10.1016/j.foodchem.2023.136136.

[18] Bao W, Tian F, Lyu C, Liu B, Li B, Zhang L, et al. Experimental and theoretical explorations of nanocarriers' multistep delivery performance for rational design and anticancer prediction. Sci Adv 2021. doi: https://doi.org/10.1126/sciadv.aba2458.

[19] Chen Y, Su W, Tie S, Cui W, Yu X, Zhang L, et al. Orally deliverable sequence-targeted astaxanthin nanoparticles for colitis alleviation. Biomaterials 2023. doi: https://doi.org/10.1016/j.biomaterials.2022.121976.

[20] Drake ZC, Seffernick JT, Lindert S. Protein complex prediction using Rosetta, AlphaFold, and mass spectrometry covalent labeling. Nat Commun 2022. doi: https://doi.org/10.1038/s41467-022-35593-8.

[21] Bottaro S, Lindorff-Larsen K. Biophysical experiments and biomolecular simulations: a perfect match? Sci 2018. doi: https://doi.org/10.1126/science.aat4010.

[22] Zang Z, Tian J, Chou S, Lang Y, Tang S, Yang S, et al. Investigation on the interaction mechanisms for stability of preheated whey protein isolate with anthocyanins from blueberry. Int J Biol Macromo 2024. doi: https://doi.org/10.1016/j.ijbiomac.2023.127880.

[23] Tian J, Liao X, Wang Y, Si X, Shu C, Gong E, et al. Identification of cyanidin-3-arabinoside extracted from blueberry as a selective protein tyrosine phosphatase 1B inhibitor. J Agr Food Chem 2019. doi: https://doi.org/10.1021/acs.jafc.9b06155.

[24] Cao Y, Xia Q, Aniya CJ, Jin Z. Copigmentation effect of flavonols on anthocyanins in black mulberry juice and their interaction mechanism investigation. Food Chem 2023. doi: https://doi.org/10.1016/j.foodchem.2022.133927.

[25] Bao C, Liu B, Li B, Chai J, Zhang L, Jiao L, et al. Enhanced transport of shape and rigidity-tuned α-lactalbumin nanotubes across intestinal mucus and cellular barriers. Nano Lett 2020. doi: https://doi.org/10.1021/acs.nanolett.9b04841.

[26] Trouillas P, Sancho-García JC, De Freitas V, Gierschner J, Otyepka M, Dangles O. Stabilizing and modulating color by copigmentation: insights from theory and experiment. Chem Rev 2016. doi: https://doi.org/10.1021/acs.chemrev.5b00507.

[27] Chang R, Chen L, Qamar M, Wang Y, Li L, Zhang J, et al. The bioavailability, metabolism and microbial modulation of curcumin-loaded nanodelivery systems. Adv Colloid Interface Sci 2023. doi: https://doi.org/10.1016/j.cis.2023.102933.

[28] Yang L, Wang Y, Li Z, Wu X, Mei J, Zheng G. Brain targeted peptide-functionalized chitosan nanoparticles for resveratrol delivery: impact on insulin resistance and gut microbiota in obesity-related Alzheimer's disease. Carbohyd Polym 2023. doi: https://doi.org/10.1016/j.carbpol.2023.120714.

[29] Moore KJ, Sheedy FJ, Fisher EA. Macrophages in atherosclerosis: a dynamic balance. Nat Rev Immunol 2013. doi: https://doi.org/10.1038/nri3520.

[30] Tian J, Zhao M, Xu J, Lv T-M, Liu X-C, Sun S, et al. Inhibitory mechanism of prenylated flavonoids isolated from mulberry leaves on α-glucosidase by multi-spectroscopy and Molecular dynamics simulation. J Agric Food Chem 2023. doi: https://doi.org/10.1021/acs.jafc.3c00776.

[31] Shibu ES, Ono K, Sugino S, Nishioka A, Yasuda A, Shigeri Y, et al. Photouncaging nanoparticles for MRI and fluorescence imaging *in vitro* and *in vivo*. ACS Nano 2013. doi: https://doi.org/10.1021/nn4043699.

[32] Rosenheim O. Observations on anthocyanins. I: the anthocyanins of the young leaves of the grape vine. Biochem J 1920. doi: https://doi.org/10.1042/bj0140178.

[33] Scott-Moncrieff R. Natural anthocyanin pigments. Biochem J 1930. doi: https://doi.org/10.1042/bj0240753.

[34] Alston RE, Hagen C. Relation of Leuco-anthocyanins to anthocyanin synthesis. Nat 1955. doi: https://doi.org/10.1038/175990a0.

[35] Wu H, Oliveira G, Lila MA. Protein-binding approaches for improving bioaccessibility and bioavailability of anthocyanins. Compr Rev Food Sci F 2022. doi: https://doi.org/10.1111/1541-4337.13070.

[36] Chen Z, Wang G, Xu Z, Wang J, Yu Y, Cai T, et al. How do distance and solvent affect halogen bonding involving negatively charged donors? J Phys Chem B 2016. doi: https://doi.org/10.1021/acs.jpcb.6b05027.

[37] Zhang H, Ju M, Hamid N, Ma Q, Shang D, Jia C, et al. Exploring the effects of whey protein components on the interaction and stability of cyanidin-3-*O*-glucoside. J Sci Food Agr 2024. doi: https://doi.org/10.1002/jsfa.13828.

[38] Pina F, Melo MJ, Laia CAT, Parola AJ, Lima JC. Chemistry and applications of flavylium compounds: a handful of colours. Chem Soc Rev 2012. doi: https://doi.org/10.1039/c1cs15126f.

[39] Chan HCS, Shan H, Dahoun T, Vogel H, Yuan S. Advancing drug discovery via artificial intelligence. Trends Pharmacol Sci 2019. doi: https://doi.org/10.1016/j.tips.2019.07.013.

[40] Felgines C, Talavéra S, Texier O, Besson C, Fogliano V, Lamaison J-L, et al. Absorption and metabolism of red orange juice anthocyanins in rats. Brit J Nutr 2006. doi: https://doi.org/10.1079/bjn20061728.

[41] Ichiyanagi T, Shida Y, Rahman MM, Hatano Y, Konishi T. Bioavailability and tissue distribution of anthocyanins in bilberry (*Vaccinium myrtillus L.*) extract in rats. J Agr Food Chem 2006. doi: https://doi.org/10.1021/jf0602370.

[42] Kurilich AC, Clevidence BA, Britz SJ, Simon PW, Novotny JA. Plasma and urine responses are lower for acylated vs nonacylated anthocyanins from raw and cooked purple carrots. J Agr Food Chem 2005. doi: https://doi.org/10.1021/jf050570o.

[43] Drucker DJ. Advances in oral peptide therapeutics. Nat Rev Drug Discov 2019. doi: https://doi.org/10.1038/s41573-019-0053-0.

[44] Lamson NG, Berger A, Fein KC, Whitehead KA. Anionic nanoparticles enable the oral delivery of proteins by enhancing intestinal permeability. Nat Biomed Eng 2019. doi: https://doi.org/10.1038/s41551-019-0465-5.

[45] Zhu Q, Chen Z, Paul PK, Lu Y, Wu W, Qi J. Oral delivery of proteins and peptides: challenges, status quo and future perspectives. Acta Pharm Sin B 2021. doi: https://doi.org/10.1016/j.apsb.2021.04.001.

[46] Zhao X, Zhang H, Li J, Tian M, Yang J, Sun S, et al. Orally administered saccharide-sequestering nanocomplex to manage carbohydrate metabolism disorders. Sci Adv 2021. doi: https://doi.org/10.1126/sciadv.abf7311.

[47] Nie T, Fang Z, Liu H, Zhang X, Ying F, Xu X, et al. Bioactive spermidine nanoparticles for effective cardiovascular recovery and diabetic therapy. Chem Eng J 2022. doi: https://doi.org/10.1016/j.cej.2022.137353.

[48] Rashwan AK, Karim N, Xu Y, Xie J, Cui H, Mozafari MR, et al. Potential micro-/nano-encapsulation systems for improving stability and bioavailability of anthocyanins: an updated review. Crit Rev Food Sci 2021. doi: https://doi.org/10.1080/10408398.2021.1987858.

[49] Liang T, Jing P, He J. Nano techniques: an updated review focused on anthocyanin stability. Crit Rev Food Sci 2023. doi: https://doi.org/10.1080/10408398.2023.2245893.

[50] Shen Y, Zhang N, Tian J, Xin G, Liu L, Sun X, et al. Advanced approaches for improving bioavailability and controlled release of anthocyanins. J Control Release 2022. doi: https://doi.org/10.1016/j.jconrel.2021.11.031.

[51] Rosales TKO, Hassimotto NMA, Lajolo FM, Fabi JP. Nanotechnology as a tool to mitigate the effects of intestinal microbiota on metabolization of anthocyanins. Antioxidants 2022. doi: https://doi.org/10.3390/antiox11030506.

[52] Alsharairi NA. Insights into the mechanisms of action of proanthocyanidins and anthocyanins in the treatment of nicotine-induced non-small cell lung cancer. international. Int J Mol Sci 2022. doi: https://doi.org/10.3390/ijms23147905.

[53] Cui Y, Yang L, Meng X, Ma J, Deng H, Liu X, et al. Cyanidin-3-galactoside from Aronia melanocarpa ameliorates PM10 induced pulmonary injury by modulating M1/M2 macrophage polarization and NRF2/Sirt1 MAPK signaling. J Funct Foods 2021. doi: https://doi.org/10.1016/j.jff.2021.104363.

[54] Liu Y, Tan D, Tong C, Zhang Y, Xu Y, Li X, et al. Blueberry anthocyanins ameliorate radiation-induced lung injury through the protein kinase RNA-activated pathway. Chem Biol Interact 2015. doi: https://doi.org/10.1016/j.cbi.2015.11.001.

[55] Ouyang S, Chen W, Gaofeng Z, Changcheng L, Guoping T, Minyan Z, et al. Cyanidin-3-*O*-β-glucoside protects against pulmonary artery hypertension induced by monocrotaline via the TGF-β1/p38 MAPK/CREB signaling pathway. Mol Med Rep 2021. doi: https://doi.org/10.3892/mmr.2021.11977.

[56] Liu S, Ma C, Zhang Y, Wang Y, Tian J, Li B, et al. Different processing methods on anthocyanin composition and antioxidant capacity in blueberry juice: based on metabolomics and DFT analysis. eFood 2024. doi: https://doi.org/10.1002/efd2.131.

[57] Willis KA, Ambalavanan N. Necrotizing enterocolitis and the gut-lung axis. Semin Perinatol 2021. doi: https://doi.org/10.1016/j.semperi.2021.151454.

[58] Zhou D, Wang Q, Liu H. Coronavirus disease-19 and the gut-lung axis. Int J Infect Dis 2021. doi: https://doi.org/10.1016/j.ijid.2021.09.013.